Gas gain and signal length measurements with a triple-GEM at different pressures of Ar-, Kr- and Xe-based gas mixtures *

A. Orthen a,*, H. Wagner a, H.J. Besch a, S. Martoiu a, R.H. Menk b, A.H. Walenta a, U. Werthenbach a

^a Universität Siegen, Fachbereich Physik, Emmy-Noether-Campus,
 Walter-Flex-Straße 3, 57068 Siegen, Germany
 ^bELETTRA, Sincrotrone Trieste, S.S. 14, km 163.5, Basovizza, 34012 Trieste,
 Italy

Abstract

We investigate the gas gain behaviour and the energy resolution of a triple-GEM configuration in gas mixtures of argon, krypton and xenon with ten and thirty percent of carbon dioxide at pressures between 1 and 3 bar. Since the signal widths affect the dead time behaviour of the detector we present signal length measurements to evaluate the use of the triple-GEM in time-resolved X-ray imaging.

PACS: 51.10.+y; 51.50.+v; 29.40.Cs

Key words: Micro pattern gaseous detectors; GEM; Gas electron multiplier; Gas gain; Signal shape; Time-resolved X-ray imaging

1 Introduction

In the recent years the application range of GEMs [1] in detector development has been widened up. Besides the operation in detectors at high energy projects like HERA-B [2] the GEM is also used in gaseous photomultiplier

^{*} Work supported by the European Community (contract no. ERBFMGECT980104).

^{*} Corresponding author. Tel.: +49 271-740-3563; fax: +49 271-740-3533; e-mail: orthen@alwa02.physik.uni-siegen.de.

development [3,4] or X-ray imaging detectors [5,6]. Thereby, the GEM is usually combined with other micro pattern devices like MSGCs [7,8], MGCs [9], micromegas [10] or MicroCAT [11]. Also the cascade of multiple GEM stages has been tested extensively [12].

A triple-GEM cascade working as a detector for solar neutrino and dark matter search has been tested at high pressure of pure noble gases [13,14]. These kinds of gaseous detectors are operated at temperatures close to the boiling temperature of the gas. Equivalent to this operation at atmospheric pressure is the operation with higher pressure (depending on the noble gas used) at room temperature. High pressure is also desired in photon detection to increase quantum efficiency. If pure noble gases are not explicitly needed it is helpful to add a quench gas fraction of up to some 10 % to the noble gases. This leads normally to smaller charge diffusion, shorter signal lengths and the possibility to obtain higher gas gains. Examinations of the gas gaining behaviour of alternative micro pattern devices like MSGCs [15] or the behaviour of a single GEM/MSGC-combination [16] in noble gas/quench gas environments show that the maximum gain drops with pressure.

The aim of the subsequent investigations is to test the performance of a triple-GEM detector at higher pressures of dense noble gas/quench gas mixtures to increase the quantum efficiency for photon detection in the energy range of $8-24\,\mathrm{keV}$. We investigate the gas gain behaviour and energy resolution at different pressures and quench gas fractions. We examine the signal lengths which mainly affect the dead time. Besides space charge effects the dead time limits the rate capability.

2 Detector setup

The schematic setup of the triple-GEM constellation is shown in Fig. 1. The individual GEM foils with dimensions of $6 \times 6 \,\mathrm{cm^2}$ are glued under slight tension to a 1 mm thick ceramic frame. The GEM type is characterised by a hole pitch of $140\,\mu\mathrm{m}$ and an optical transparency of $12\,\%$; the thickness of the GEM amounts to $60\,\mu\mathrm{m}$ including two copper layers of $5\,\mu\mathrm{m}$ each and a Kapton foil of $50\,\mu\mathrm{m}$ thickness.

We have decided to use a distance between the GEMs of 2 mm. The lowermost GEM is mounted at a distance of 1 mm above the readout structure. Following the usual nomenclature we denote the applied electric field between the GEMs by transfer field and the field between the lowermost GEM and the readout structure by induction field. Above the GEM configuration a drift cage is mounted which provides a homogeneous drift field in the conversion region above the uppermost GEM with a depth of 27 mm.

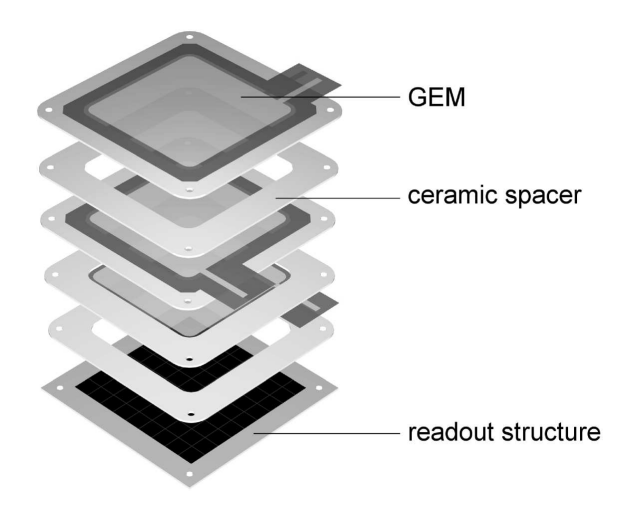


Fig. 1. Schematic setup of the triple-GEM configuration.

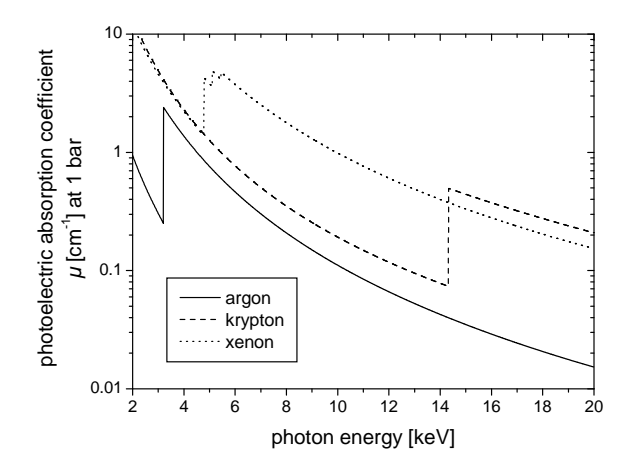


Fig. 2. Photoelectric absorption coefficient μ in 1 bar argon, krypton and xenon [19].

For the gas gain measurements the position sensitive resistive readout structure [17,18] has been replaced by a copper anode with a size corresponding to the GEM foils. The signal examination has been carried out with a smaller copper anode ($\approx 1\,\mathrm{cm}^2$) to reduce the capacitance and therefore to enhance the response of the preamplifier.

The 1 mm thick carbon fibre entrance window of the pressure vessel accepts pressures up to about 3 bar. To achieve high quantum efficienty for photon detection in the energy range of $5-14\,\mathrm{keV}$ xenon is preferably used (compare to Fig. 2). For photons in the energy range between about 14 and 24 keV quantum efficiency increases using krypton.

3 Gas gain measurements

In the following section we present results of gas gain measurements in the triple-GEM configuration. The effective gas gain G_{eff} is defined as the product of the real gas gain G_{GEM} and the electron transparencies $\varepsilon_{1\text{-GEM}}$ and $\varepsilon_{2\text{-GEM}}$ of all GEMs [11]:

$$G_{\text{eff}} = \prod_{i=1}^{3} \varepsilon_{1\text{-GEM-i}} \varepsilon_{2\text{-GEM-i}} G_{\text{GEM-i}} , \qquad (1)$$

where $\varepsilon_{1\text{-GEM-i}}$ is the probability, that the electrons, coming from the drift/conversion region, reach the multiplication region in the centre of a hole in GEM #i; $\varepsilon_{2\text{-GEM-i}}$ is the probability, that these electrons reach the subjacent GEM or anode. The effective gain G_{eff} is experimentally determined by the quotient of the measured current at the anode I_{anode} and the "incoming" current I_0 :

$$G_{\text{eff}} = \frac{I_{\text{anode}}}{I_0} \ . \tag{2}$$

The current

$$I_0 = Re \frac{E_{\gamma}}{W} \tag{3}$$

is determined by the conversion rate R of the X-ray photons in counting mode of the detector, by the photon energy E_{γ} and by the average energy required to produce one electron-ion pair in the gas W; e denotes the elementary charge.

In fact, the incoming current I_0 is overestimated – at least at small drift fields and high gas pressures – because of charge losses due to recombination and attachment in the conversion region. This effect, which is mainly a three-body process and therefore increases with the square of the gas pressure, is shown as an example in Fig. 3 in a Xe/CO₂ (90/10) gas mixture at pressures between 1 and 2 bar. At drift fields larger than about 1000 V/cm the effective pulse height reaches a plateau. In this region attachment and recombination is negligible and the incoming current I_0 is described correctly by Eq. (3).

Since the maximum voltage applied to the drift cathode was restricted by the detector geometry to around $-(6000 \pm 500)\,\mathrm{V}$ we have chosen a drift field of $400\,\mathrm{V/cm}$ to prevent the detector from sparking at the drift cathode and to have enough margin to increase more crucial potentials like GEM operation voltages. The transfer fields have been chosen to $2500\,\mathrm{V/cm}$, and we have applied an induction field of $3000\,\mathrm{V/cm}$ to avoid full discharge propagation [20]. Furthermore, we have set the GEM voltages such, that the uppermost GEM voltage is $10\,\%$ higher than the voltage of the middle GEM; the lowermost GEM is set to an operation voltage $10\,\%$ smaller than the "reference" voltage

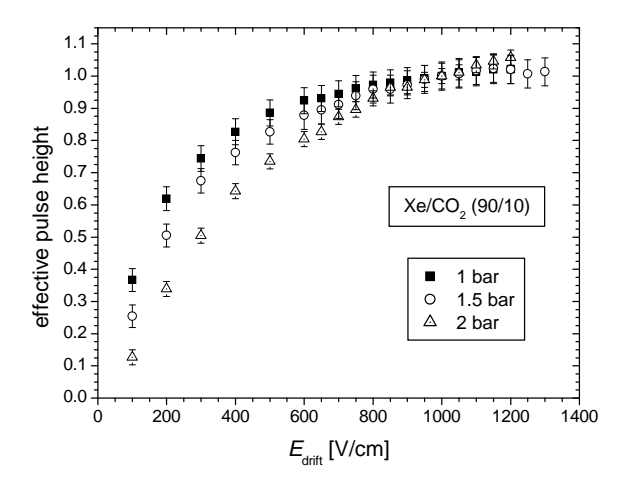


Fig. 3. Effective pulse height as a function of the applied drift field in $\rm Xe/CO_2$ (90/10) for a transfer field of 2500 V/cm and an induction field of 3000 V/cm.

of the middle GEM $\Delta U_{\rm GEM2}$. This setting assures minimum discharge rates [20]. The sum of all applied GEM voltages always amounts to $3 \Delta U_{\rm GEM2}$.

For illumination with X-ray photons we have used a 55 Fe source, emitting photons with an energy of $5.9\,\mathrm{keV}$ and with a rate of $41\,\mathrm{kHz}$ collimated to about $28\,\mathrm{mm}^2$.

The gas gain measurements were limited by sparks. We stopped the measurements at spark rates $\gtrsim 2 \, \text{sparks/min}$, which is rather an arbitrary limit. Important, however, is the stable detector operation at slightly lower voltages and hence lower gas gains.

In the following subsections we compare our results with triple-GEM gas gain measurements in pure noble gas environments [13,14].

3.1 Gas gain in Ar/CO_2 (70/30)

Although argon gas mixtures are not well suited for photon detection in the energy range above a few tens of keV we have carried out gas gain measurements in $\rm Ar/CO_2$ (70/30) to compare the results to published data and to our results achieved with Kr- and Xe-mixtures. The measured effective gain is shown in Fig. 4. The maximum gas gain achievable decreases with pressure.

In comparison, the maximum gain at a pressure of 3 bar is about 10 times smaller than in pure argon [13] whereas we achieve higher gains at atmospheric pressure.

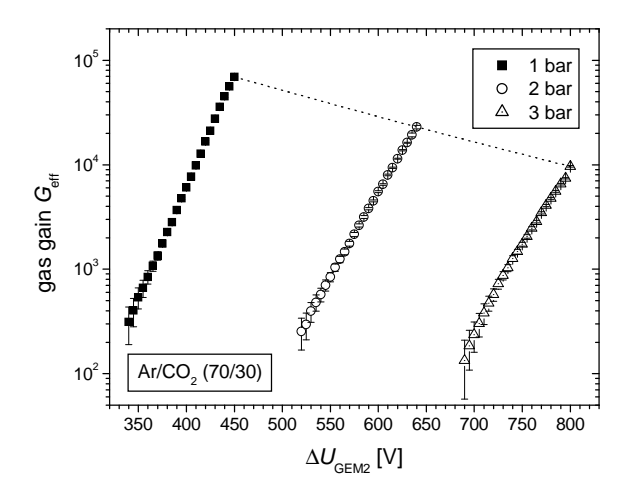


Fig. 4. Effective gas gain as a function of the applied voltage at the middle GEM $\Delta U_{\rm GEM2}$ in Ar/CO₂ (70/30) at pressures of 1, 2 and 3 bar. The voltages applied to the first and third GEM have been changed proportionally.

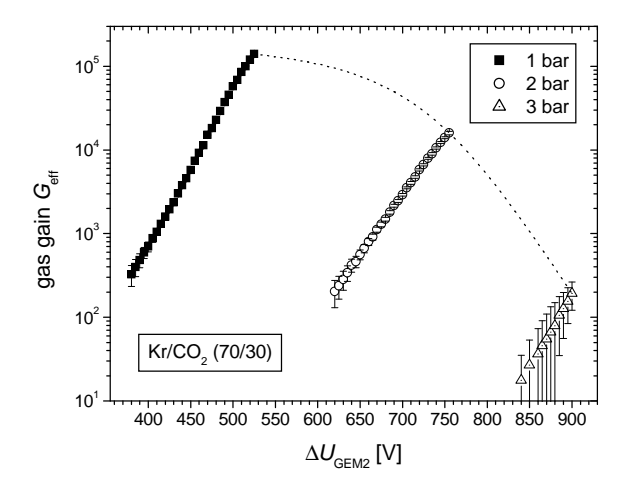


Fig. 5. Effective gas gain as a function of the applied voltage at the middle GEM $\Delta U_{\rm GEM2}$ in Kr/CO₂ (70/30) at pressures of 1, 2 and 3 bar.

3.2 Gas gain in Kr/CO₂ mixtures

We have investigated two Kr-mixtures with different CO_2 fractions of 30 % (see Fig. 5) and 10 % (see Fig. 6), respectively. In both mixtures the effective gain exceeds 10^4 up to pressures of 2 bar. Nevertheless, a quench gas fraction of 30 % is not well suited for operation at pressures > 2 bar where we obtained a strong decrease in gas gain to about 200. In contrast to that still large gas gains in the order of $5 \cdot 10^3$ are possible with a carbon dioxide fraction of 10 %.

The comparison to gas gain measurements in pure krypton shows that the addition of CO_2 leads to much higher possible gas gains ($\approx 10^5$) at atmospheric pressure than in pure krypton ($\approx 10^4$) [14]. At a pressure of 3 bar we obtained lower gain with a fraction of 30 % CO_2 and higher gain with a fraction of 10 %

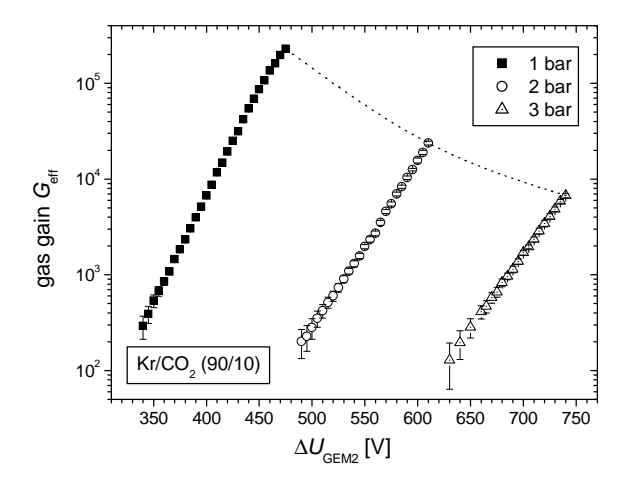


Fig. 6. Effective gas gain as a function of the applied voltage at the middle GEM $\Delta U_{\rm GEM2}$ in Kr/CO₂ (90/10) at pressures of 1, 2 and 3 bar.

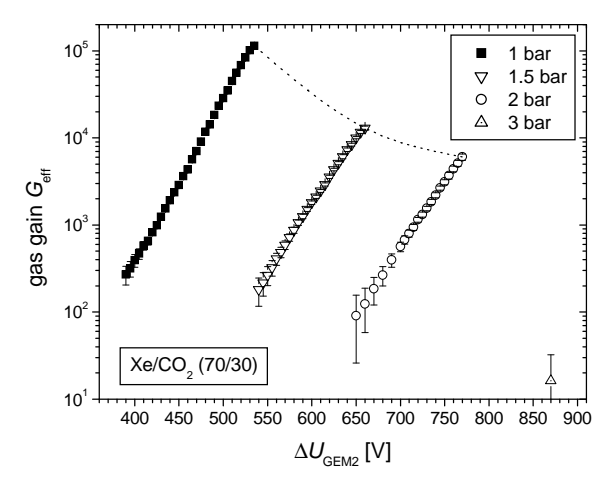


Fig. 7. Effective gas gain as a function of the applied voltage at the middle GEM $\Delta U_{\rm GEM2}$ in Xe/CO₂ (70/30) at pressures of 1, 1.5, 2 and 3 bar.

 CO_2 compared to pure krypton ($\approx 10^3$).

3.3 Gas gain in Xe/CO_2 mixtures

The use of Xe-based gas mixtures offers the largest quantum efficiency for photon detection in the energy range between 5 and 14 keV. Results of gas gain measurements for $\rm Xe/CO_2$ (70/30) and $\rm Xe/CO_2$ (90/10) are shown in Fig. 7 and Fig. 8. Like for Ar- and Kr-gas mixtures an amount of 10 % carbon dioxide enables operation with gas gains $> 10^3$ at pressures above 2 bar. High quencher fractions are also not well suited for pressure operation with xenon.

At a pressure of 3 bar we measured a maximum gain of $\approx 10^3$ with a fraction of 10% of carbon dioxide which is higher compared to the maximum gain in pure xenon ($\approx 5 \cdot 10^2$) [13]. At atmospheric pressure we obtained with both

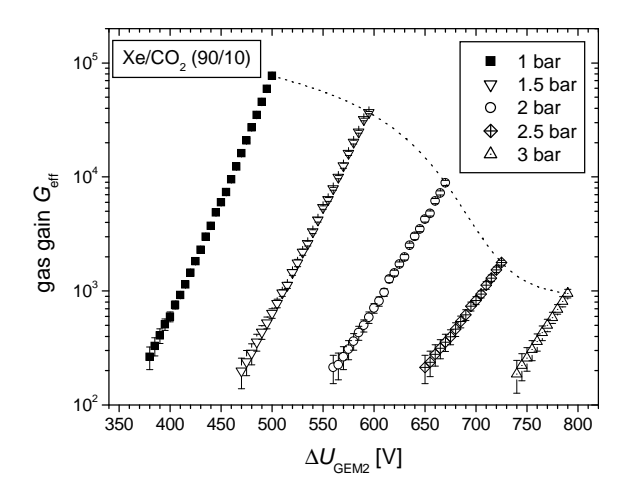


Fig. 8. Effective gas gain as a function of the applied voltage at the middle GEM $\Delta U_{\rm GEM2}$ in Xe/CO₂ (90/10) at pressures of 1, 1.5, 2, 2.5 and 3 bar.

quench gas fractions gas gains which are about 10 times higher than in pure xenon.

3.4 Homogeneity

Theoretically, the relative energy resolution $\sigma(E)/E$ of any gaseous detector can be described by the following equation:

$$\left(\frac{\sigma(E)}{E}\right)^2 = \frac{a^2}{E^2} + \frac{b^2}{E} + c^2,$$
 (4)

where E denotes the photon energy. Assuming the convolution of independent contributions all terms in Eq. (4) add quadratically. The first term describes a constant energy-independent contribution to the standard deviation of the measured energy $\sigma(E)$, i.e. due to electronic noise of the readout electronics. The second term is due to statistic fluctuations of the produced number of charge carriers in the detected charge. The coefficient b in Eq. (4) can be expressed by $b^2 = W(F+f)$ [21], where W denotes the average energy required to produce one electron-ion pair in the gas, F the Fano factor [22] and f the relative variance of the gas gain. Typical values for F are 0.17 in argon [23] and values between 0.4 and 1 for f in proportional counters [24], depending on gas, pressure, geometry of the detector and applied electric fields. Finally, the last term, which contributes constantly to the relative energy resolution, describes systematic influences like recombination or attachment or gain variations due to variable operating conditions, e.g. pressure variations.

We have measured the local and the global energy resolution of the triple-GEM constellation at different pressures of $\rm Ar/CO_2$ (70/30) (see Fig. 9), where we define local energy resolution as the energy resolution obtained by irradiation

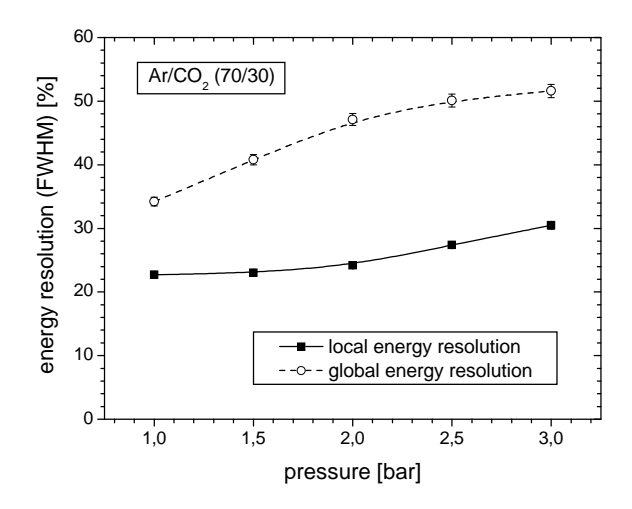


Fig. 9. Local and global energy resolution as a function of gas pressure in $\rm Ar/CO_2$ (70/30). We applied a drift field of $\rm 1\,kV/cm$, a transfer field of $\rm 2.5\,kV/cm$ and an induction field of $\rm 3\,kV/cm$.

with a 55 Fe source collimated to $12\,\mathrm{mm^2}$. We define global energy resolution as the energy resolution obtained by illuminating the whole detector area of $6\times 6\,\mathrm{cm^2}$. The comparison of local and global energy resolution will mostly affect the third term in Eq. (4) and therefore allows the separation of the major systematic errors. The mean gas gain in all measurements has been kept constant to about 5000. During the measurements the gain slightly decreased as a function of time due to charging of the insulating Kapton in the GEM. A quantitative description of the influence of this effect on the measured energy resolution is difficult because the charging was found to be dependent on illumination time and position, photon flux and dryness of the Kapton surface.

Both, the local and the global energy resolution deteriorate with increasing gas pressure, which may be explained as follows:

- \bullet possible increase of the Fano factor F at higher pressure [25].
- increase of the relative variance of the gas gain f.
- larger recombination of electrons and ions or attachment to electro-negative impurities which means that the second and third term in Eq. (4) increase.

The deviations in energy resolution between local and global illumination is due to several aspects: First, the GEMs, themselves, produce intrinsic gain inhomogeneities since all holes (and thus the gain) are slightly different. Furthermore, the distance between the individual GEMs and the distance between undermost GEM and anode is not constant over all the detector area, which leads to transfer and induction field inhomogeneities und finally to variations in the charge transfer behaviour and in the effective gas gain of the GEM (compare to Eq. (1)). Figure 10 shows the relative effective gain measured along the vertically centred x-axis. Gain variations of up to 25 % become obvious.

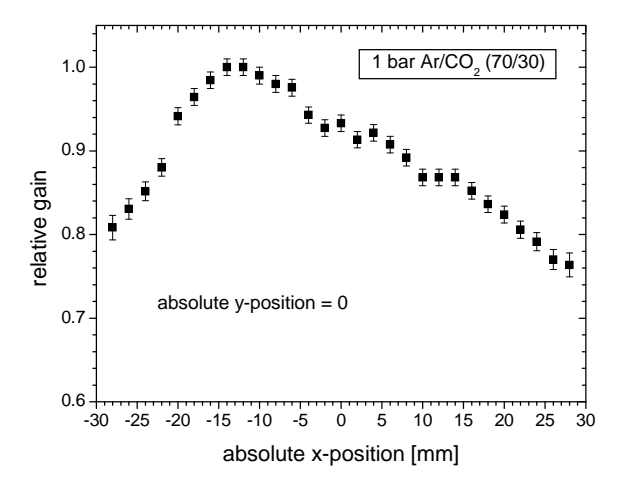


Fig. 10. Relative effective gain along the vertically centred x-axis of the detector in Ar/CO_2 (70/30).

3.5 Discussion

We have measured the gas gain behaviour at different pressures of argon, krypton and xenon with additions of 10 % and 30 % of carbon dioxide. Thereby, a strong influence of the quench gas fraction becomes obvious. It is definitely a non-trivial task to optimise the quench gas fraction at a given pressure due to a complicated interplay of these parameters. Generally, the maximum gas gain of the triple-GEM achievable in slightly quenched nobel gas mixtures is higher than in pure nobel gases. Higher pressure demands for smaller quench gas fractions.

The strong influence of the quencher fraction indicates, that a stable avalanche process is not only based on electron-induced ionization of gas atoms. The UV-photons which are produced in the avalanche development may contribute noticeably to the multiplication procedure. With increasing pressure and constant (or even larger) quench gas fraction the range of the UV-photons is decreasing. For instance, the deterioration in energy resolution in a MWPC is stopped when a very small quench gas fraction of only 2% at very high pressures (up to 30 bar) is added to argon [26]. However, still smaller fractions of quenching gas lead to an unsafe operation of the detector.

A good choice for photon detection with the triple-GEM is the use of $\rm Xe/CO_2$ (90/10) at pressures between 1 and 2 bar. Gas gains of $\rm 5 \cdot 10^3$ can be easily reached without sparking. For still higher pressures of xenon based gas mixtures the detector response with a smaller amount (< 10 %) of quenching gas should be taken into consideration.

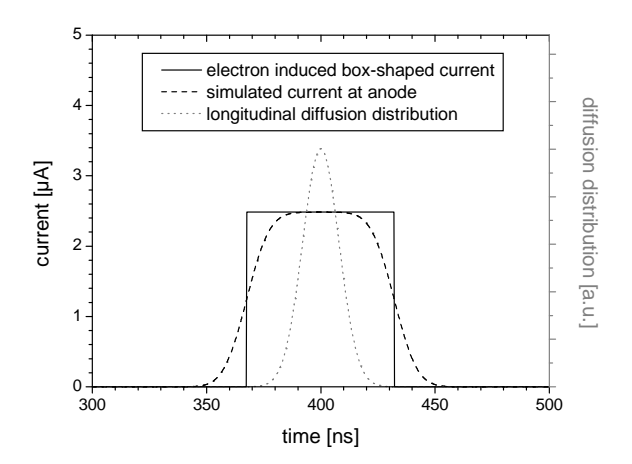


Fig. 11. Schematic simulation of a signal shape in the triple-GEM geometry. The solid line displays the current induced by a charge cluster with δ -like spatial distribution, moving with constant velocity from one electrode towards a parallel electrode. The dashed line shows the expected anode current as a result of the convolution with a longitudinal diffusion spreading (dotted line) of the real charge cluster.

4 Signal length investigations

We have studied the dependence of the anode signal shape on GEM voltage, induction field, transfer field and drift field for all gas mixtures and several pressures since dead time of the detector is mainly determined by the signals lengths. The copper readout anode for these measurements has a size of $1 \times 1 \text{ cm}^2$. The integrating preamplifier and the shaper including a pole-zero filter to cancel the pole of the integrating first stage are in-house developments. The δ -response of this amplification system is gaussian-like with a width of 15 ns (fwhm) due to bandwidth limitations.

The anode signal shape is mainly determined by two aspects:

- (1) A spatially δ -like distributed electron cluster moving from the bottom side of the undermost GEM towards the readout structure induces a box-shaped current at both involved electrodes (see box-shaped current in Fig. 11) if the electric field and therefore the electron drift velocity in the region of interest is assumed to be constant [27]. The copper-clad bottom side of the GEM shields all currents induced by charge movements appearing above this electrode; especially the slow ions do not contribute to the signal shape. The crucial parameters for the width of the box-shaped current are the electron velocity in the electric field of the induction region and the distance between the bottom side of the GEM and the anode which was set to 1 mm in our case.
- (2) The longitudinal diffusion σ_l of the primary produced electrons (photoelectron plus subsequently produced ≈ 300 electrons for 8 keV photons in argon) in the conversion region leads to a gaussian smearing (see dotted

line in Fig. 11) of this box function (convolution result see dashed line in Fig. 11). The width of the gaussian

$$\sigma_{\rm t} = \left(\sigma_{\rm l0} \, \overline{\sqrt{l}}\right) / v_{\rm e} \tag{5}$$

is determined by the longitudinal diffusion coefficient σ_{10} and the electron drift velocity $v_{\rm e}$ in the applied drift field and gas mixture used and finally by the mean drift path \sqrt{l} of the electrons, which is dependent on photon energy, maximum drift length and absorption coefficient of the gas. An additional contribution comes from the longitudinal electron diffusion in the transfer regions between the GEMs. In our simulation this contribution has also been taken into account.

For most gas mixtures and pressures in our detector setup diffusion spreading is the main contribution so that the signal shape is very much gaussian-like. Due to this gaussian signal shape and the gaussian δ -response of the preamplifier/shaper-system the real signal length can be calculated to be the width of the deconvolution of both gaussians:

$$\Delta_{\text{sig-real}}^2 = \Delta_{\text{sig-meas}}^2 - \Delta_{\delta\text{-response}}^2, \tag{6}$$

where Δ is the full width half maximum of the signal. In case the measured signal shape is not gaussian (which means that the main contribution of the signal is due to the electron induced box-shaped current) Eq. (6) is no longer valid. But in this case the measured signal width is very much larger than the width of the δ -response ($\Delta_{\text{sig-meas}} \gg \Delta_{\delta\text{-response}}$) and therefore the real signal width can be determined to be $\Delta_{\text{sig-meas}} \approx \Delta_{\text{sig-meas}}$.

We have measured the full width half maximum (fwhm) of the anode signals and the δ -response with a digital oscilloscope, afterwards averaging the widths of several signals. All measurements have been performed with a transfer field of 2500 V/cm and an induction field of 3000 V/cm if not noted otherwise. The ⁵⁵Fe source has been collimated to about 12 mm²; photons were emitted with a rate of a few hundred Hz. We have carried out all signal width simulations only for 1 bar Ar/CO₂ (70/30), where experimental data on drift velocities [28] and simulated data on longitudinal diffusion [29,30] have been used.

4.1 Influence of GEM operation voltage

No influence of the GEM voltage on the signal length has been measured. The range of the investigated GEM voltages was limited by the dynamic range of the preamplifier. Anyway, the setting of the GEM voltage is determined by the desired gas gain and is therefore no freely adjustable parameter for optimisation of the signal lengths.

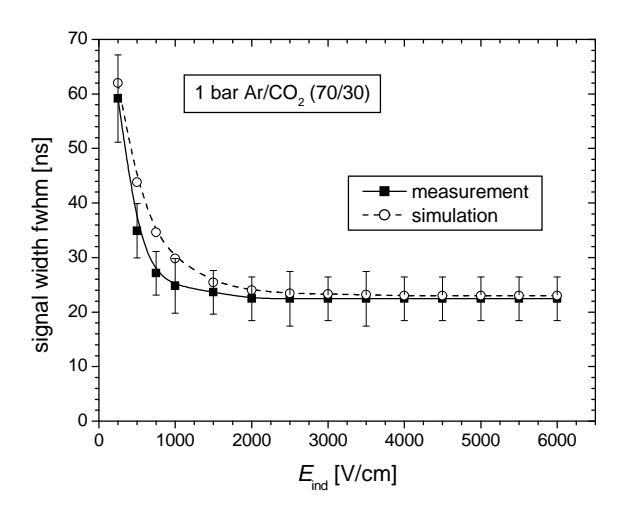


Fig. 12. Comparison between measured and simulated signal widths (fwhm) as a function of the induction field in 1 bar $\rm Ar/CO_2$ (70/30) with a constant drift field of $E_{\rm drift} = 900 \, \rm V/cm$.

4.2 Influence of the induction field

The contribution of the width of the box-shaped current to the total width of the signal increases for very small induction fields because of the decreasing electron drift velocity. Three-dimensional field calculations with Maxwell [31] using a geometry of 1 mm transfer gap, the GEM foil and 1 mm induction gap (the geometry of the GEM and more simulation details are described in Ref. [11]) show that the electric field in the induction region along the symmetry axis of a GEM hole is larger than the quotient $E = U_{\text{GEM-bottom}}/d$ of the applied voltage on the bottom side of the GEM $U_{\text{GEM-bottom}}$ and the distance d between GEM bottom and anode. This effect is some relict due to the very high electric field in the holes. The calculated width of the electron induced box-shaped current is determined by introducing a constant electron mobility for 1 bar Ar/CO₂ (70/30) as $\mu_e = 3 \cdot 10^{-3} \, \text{cm}^2/(\text{V}\mu\text{s})$ for electric fields up to 2 kV/cm and a constant velocity of $v_e = 6 \text{ cm}/\mu \text{s}$ for electric fields > 2 kV/cm. This model is a coarse parametrisation of measured electron drift velocities [28]. From the hereby determined electron velocities a mean drift velocity in the induction region is calculated. The results of this simulation and the comparison to experiment is shown in Fig. 12. A good agreement becomes obvious. The deviation at induction fields between 500 V/cm and 1500 V/cm are probably due to the coarse electron drift velocity parametrisation. At induction fields larger than about 2000 V/cm the influence of the box-shaped current becomes negligible compared to the contribution of the longitudinal electron diffusion in the conversion region.

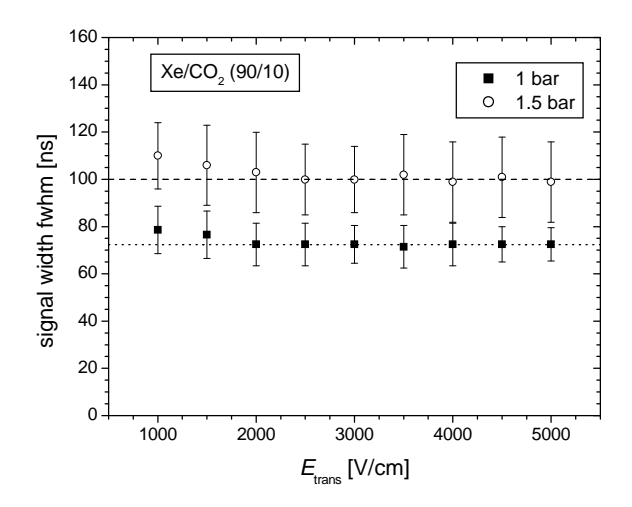


Fig. 13. Signal widths (fwhm) as a function of the transfer field between the uppermost and the middle and between the middle and the undermost GEM in 1 and $1.5 \,\mathrm{bar} \,\mathrm{Xe/CO_2} \,(90/10)$ with a constant drift field of $E_{\mathrm{drift}} = 1000 \,\mathrm{V/cm}$.

4.3 Influence of the transfer field

The measured results are shown in Fig. 13. Transfer fields smaller than $2500 \,\mathrm{V/cm}$ result in a slight increase of the signal width which can be explained by a larger longitudinal diffusion contribution from the transfer regions between the GEMs due to smaller electron drift velocities (compare to Eq. (5)). At larger transfer fields the signal width reaches a plateau.

4.4 Influence of the drift field

This section contains an intensive investigation of the influence of the applied drift field on the signal width.

The comparison between measurement and simulation (see Fig. 14) shows a good agreement for drift fields $\gtrsim 200\,\mathrm{V/cm}$. It turned out that signal width measurements at small drift fields are very difficult because the signal shape is not continuous. It is rather divided into single electron clusters reaching the anode one by one (see Fig. 15). Therefore, the error is relatively large when determining the signal length. Furthermore, a large part of the primary produced electrons is lost due to recombination and attachment at low drift fields (compare to Fig. 3) thus increasing the influence of noise. For larger drift fields the measured signal shape becomes continuous and smooth (see Fig. 16).

The measured signal widths for different gas mixtures and gas pressures are shown in Fig. 17–21. Generally, high drift fields are needed to produce short

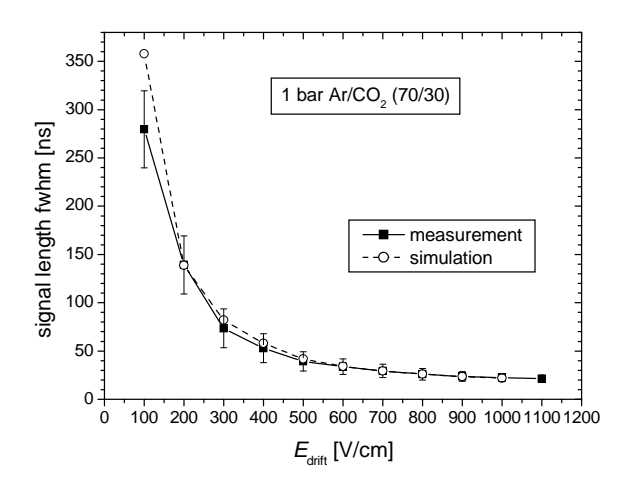


Fig. 14. Comparison between measured and simulated signal widths (fwhm) as a function of the drift field in 1 bar ${\rm Ar/CO_2}$ (70/30).

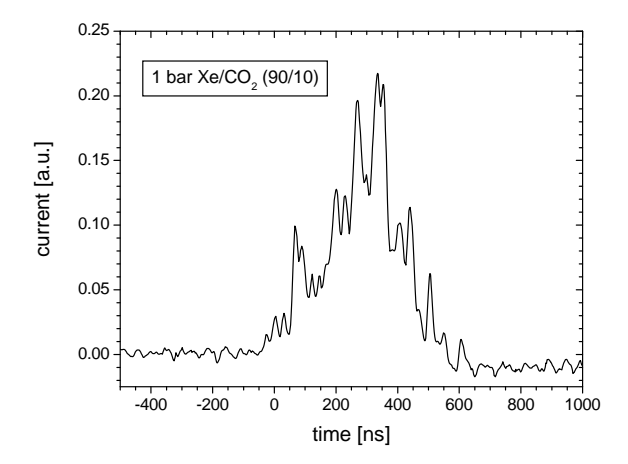


Fig. 15. Measured signal shape at a small drift field of 200 V/cm in 1 bar $\rm Xe/CO_2$ (90/10).

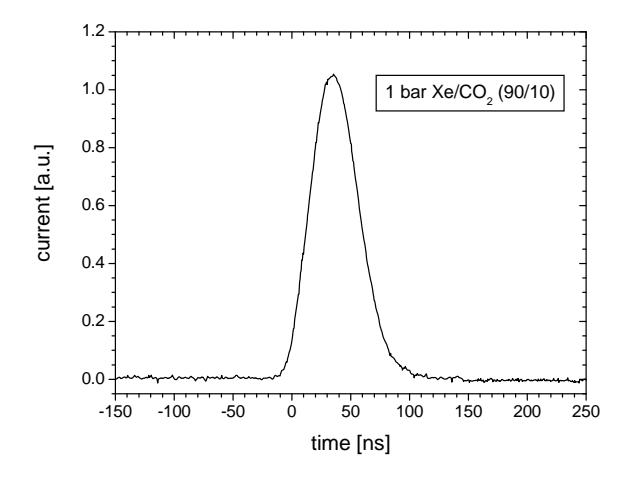


Fig. 16. Measured signal shape at a large drift field of 1000 V/cm in 1 bar $\rm Xe/CO_2$ (90/10).

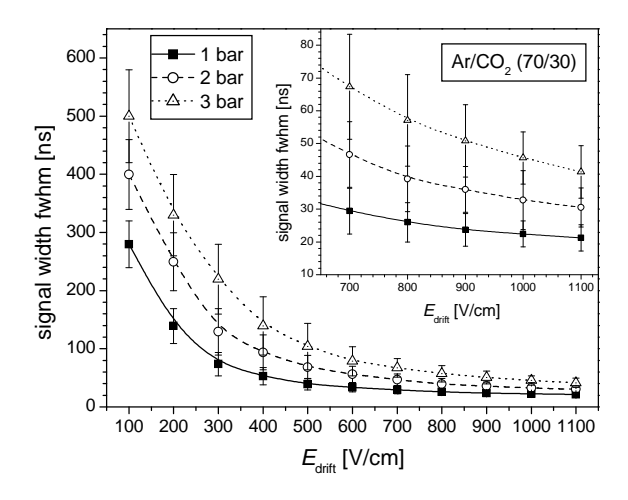


Fig. 17. Measured signal widths (fwhm) as a function of the drift field in 1,2 and 3 bar $\rm Ar/CO_2$ (70/30).

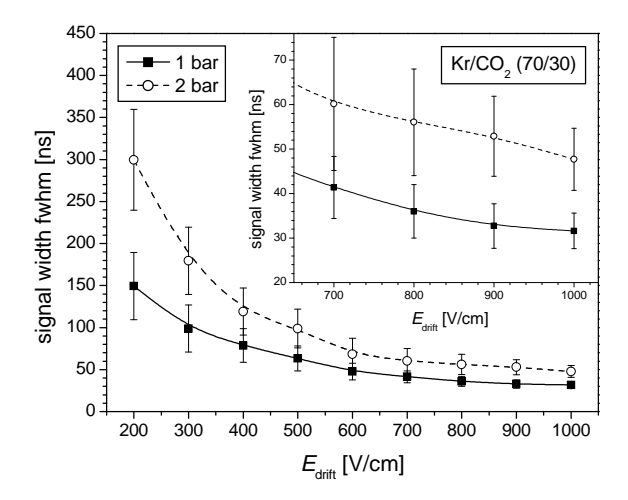


Fig. 18. Measured signal widths (fwhm) as a function of the drift field in 1 and 2 bar $\rm Kr/CO_2$ (70/30).

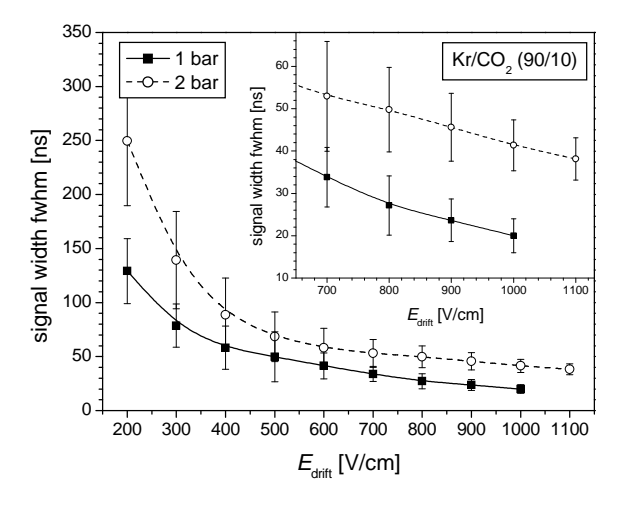


Fig. 19. Measured signal widths (fwhm) as a function of the drift field in 1 and 2 bar $\rm Kr/CO_2$ (90/10).

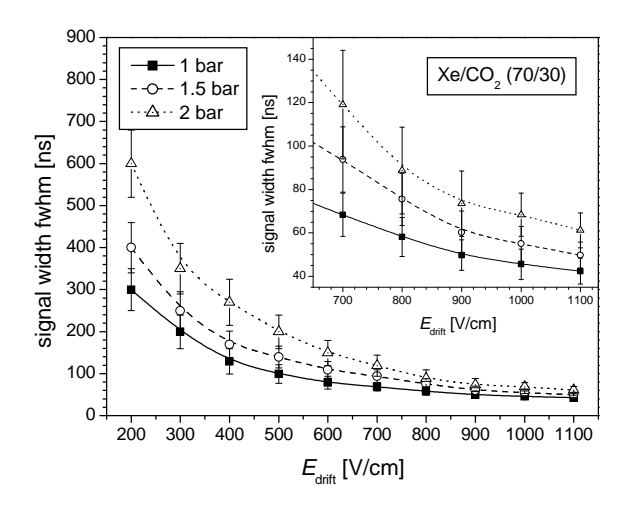


Fig. 20. Measured signal widths (fwhm) as a function of the drift field in 1, 1.5 and $2 \,\mathrm{bar} \,\mathrm{Xe/CO_2}$ (70/30).

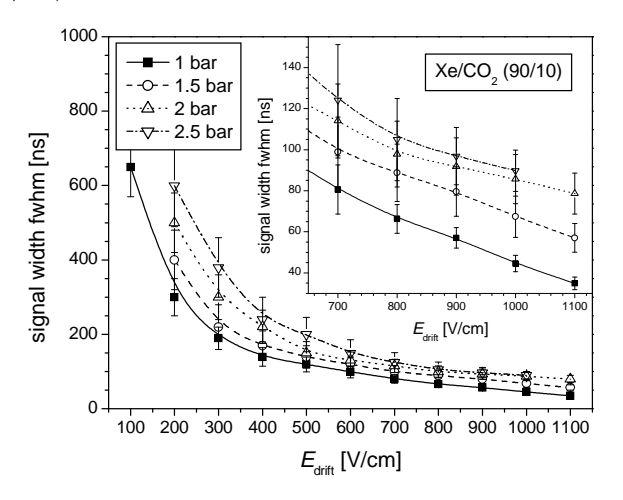


Fig. 21. Measured signal widths (fwhm) as a function of the drift field in 1, 1.5, 2 and 2.5 bar $\rm Xe/CO_2$ (90/10).

signals. We were limited to about $1000-1200\,\mathrm{V/cm}$ due to sparking at the drift cathode. The fastest signals with a signal length of < 25 ns (fwhm) are produced in the argon mixture at standard pressure (see Fig. 17). Larger pressure always increases the signal width because of decreasing drift velocities. But even in 1.5 bar $\mathrm{Xe/CO_2}$ (90/10) the signal width does not exceed 60 ns (fwhm) at a drift field of $1100\,\mathrm{V/cm}$.

4.5 Discussion

In our detector setup the drift field has the most crucial influence on the signal length although for smaller conversion regions this parameter becomes less important due to smaller longitudinal electron diffusion. The drift field should be chosen as large as allowed by the detector setup. However, the drift

field should not be too high ($\lesssim 2\,\mathrm{kV/cm}$) because the uppermost GEM loses transparency for too high drift fields [12]. The GEM operation voltage, which is mainly determined by the desired gas gain, does not influence the signal widths visibly. Transfer and induction fields $\gtrsim 2\,\mathrm{kV/cm}$ minimise the widths of the signal. If the contribution of the electron induced box-shaped current (see Fig. 11) becomes noticeable the distance between the undermost GEM and the anode can be reduced, i.e. to 0.5 mm. This should suppress this effect.

5 Conclusion

We have measured the gas gain in a triple-GEM geometry for pressures up to 3 bar of $\rm Ar/CO_2$ (70/30), $\rm Kr/CO_2$ (70/30), $\rm Kr/CO_2$ (90/10), $\rm Xe/CO_2$ (70/30) and $\rm Xe/CO_2$ (90/10). At a pressure of > 2 bar the addition of 10 % of carbon dioxide to the noble gases leads to higher maximum gas gains compared to pure noble gases. Too large amounts of quench gas disturbs operation at high pressure and is therefore not preferable. Generally, we have obtained that the quench gas fraction should decrease with pressure.

The measured signal lengths at high drift fields are in all gas mixtures investigated smaller than about $100\,\mathrm{ns}$ (fwhm). If transfer and induction fields exceed $2\,\mathrm{kV/cm}$ the signal widths get to mimimum.

Further optimisation with respect to an increased high rate behaviour can be performed with exact knowledge of photon energy and desired quantum efficiency. For example, with a desired quantum efficiency of 90 % for 8 keV-photons in 1.5 bar Xe/CO₂ (90/10) it is sufficient to have a maximum drift length of 11 mm with mean drift path $\left(\sqrt{l_{11}}\right)^2$ (see Fig. 22) instead of 27 mm with mean drift path $\left(\sqrt{l_{27}}\right)^2$ used for measurements described in this paper. The longitudinal diffusion and consequently the signal width will thus decrease by a factor of $\sqrt{l_{27}}/\sqrt{l_{11}}\approx 1.8$.

In combination with the resistive readout structure it is proposed to integrate about 90 % of the charge to achieve optimum spatial resolution [18]. Compared to the signal length fwhm, presented here, the charge integration time from 5 % to 95 % of the original signal can be calculated to be $\tau_{5-95\%} \approx 1.4 \tau_{\rm fwhm}$. Due to charge diffusion on the readout structure the charge integration time for signals with a width of $\tau_{5-95\%} = 92 \, \rm ns$ is stretched to about $\tau_{\rm rs:5-95\%} = 150 \, \rm ns$. Compared to the geometry of MicroCAT- or micromegas-detectors the triple-GEM constellation offers faster signals since only the electrons and not the slow ions contribute to the signal shape.

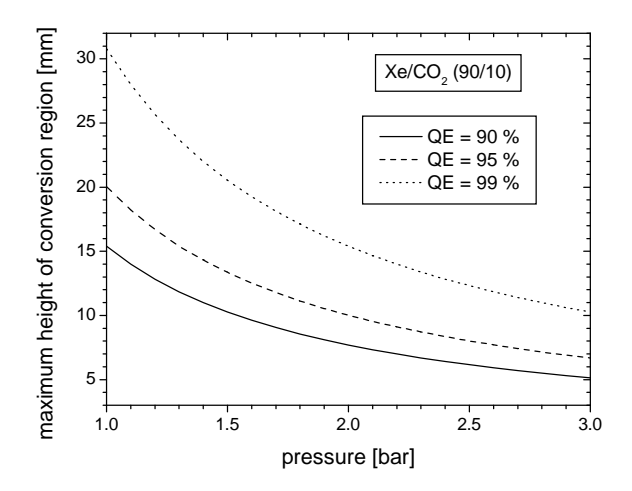


Fig. 22. Calculated maximum depth of the conversion gap as a function of pressure in Xe/CO₂ (90/10) to reach a quantum efficieny of 90 %, 95 % and 99 %, respectively, for photon energies of $E_{\gamma}=8\,\mathrm{keV}$.

Acknowledgements

We are grateful to the inner tracker group of the HERA-B collaboration for providing several GEM foils. We thank C. Fiorini for providing the preamplifier design.

References

- [1] F. Sauli. GEM: A new concept for electron amplification in gas detectors, Nucl. Instr. and Meth. A 386 (1997) 531
- [2] T. Zeuner. The MSGC-GEM Inner Tracker for HERA-B, Nucl. Instr. and Meth. A 446 (2000) 324
- [3] A. Buzulutskov, A. Breskin, R. Chechik, G. Garty, F. Sauli, L. Shekhtman. The GEM photomultiplier operated with noble gas mixtures, Nucl. Instr. and Meth. A 443 (2000) 164
- [4] A. Buzulutskov, A. Breskin, R. Chechik, G. Garty, F. Sauli, L. Shekhtman. Further studies of the GEM photomultiplier, Nucl. Instr. and Meth. A 442 (2000) 68
- [5] M. Li, M.S. Dixit, P. Johns Photon-counting digital radiography using highpressure xenon filled detectors, Nucl. Instr. and Meth. A 471 (2001) 215
- [6] S. Bachmann, S. Kappler, B. Ketzer, T. Müller, L. Ropelewski, F. Sauli, E. Schulte. High rate X-ray imaging using multi-GEM detectors with a novel readout design, Nucl. Instr. and Meth. A 478 (2002) 104

- [7] Y. Benhammou, J.M. Brom, J.C. Fontaine, D. Huss, F. Jeanneau, A. Lounis, I. Ripp-Baudot, A. Zghiche. Comparative studies of MSGC and MSGC-GEM detectors, Nucl. Instr. and Meth. A 419 (1998) 400
- [8] O. Baruth, S. Keller, U. Werthenbach, G. Zech, T. Zeuner. Sparks in MSGC and GEM detectors and a robust alternative, Nucl. Instr. and Meth. A 454 (2000) 272
- [9] P. Fonte, V. Peskov, B.D. Ramsey. Rate and gain limitations of MSGCs and MGCs combined with GEM and other preamplification structures, Nucl. Instr. and Meth. A 419 (1998) 405
- [10] S. Kane, J. May, J. Miyamoto, I. Shipsey. A study of micromegas with preamplification with a single GEM, Proceeding for the International conference on advanced technology and particle physics, Villa Olmo, Como, Italy, Oct 15-19 (2001), submitted to World Scientific (2002)
- [11] A. Orthen, H. Wagner, H.J. Besch, R.H. Menk, A.H. Walenta, U. Werthenbach. Investigations of an optimised MicroCAT, a GEM and their combination by simulations and current measurements, Nucl. Instr. and Meth. (2003), in press
- [12] S. Bachmann, A. Bressan, L. Ropelewski, F. Sauli, A. Sharma, D. Mörmann. Charge amplification and transfer processes in the gas electron multiplier, Nucl. Instr. and Meth. A 438 (1999) 376
- [13] A. Bondar, A. Buzulutskov, L. Shekhtman. High pressure operation of the triple-GEM detector in pure Ne, Ar and Xe, Nucl. Instr. and Meth. A 481 (2002) 200
- [14] A. Bondar, A. Buzulutskov, L. Shekhtman, V. Snopkov, A. Vasiljev. Triple GEM operation in compressed He and Kr, Nucl. Instr. and Meth. A 493 (2002)
- [15] L. Shekhtman, F. Angelini, R. Bellazzini, A. Brez, M.M. Massai, G. Spandre, M.R. Torquati. Performance of the gas microstrip chamber at high pressure, Proceedings of the European Workshop on X-Ray Detectors for Synchrotron Radiation Sources. Aussois (1991) 96
- [16] A. Bondar, A. Buzulutskov, F. Sauli, L. Shekhtman. High- and low-pressure operation of the gas electron multiplier, Nucl. Instr. and Meth. A 419 (1998) 418
- [17] H.J. Besch, M. Junk, W. Meissner, A. Sarvestani, R. Stiehler, A.H. Walenta. An interpolating 2D pixel readout structure for synchrotron X-ray diffraction in protein crystallography, Nucl. Instr. and Meth. A 392 (1997) 244
- [18] H. Wagner, H.J. Besch, R.H. Menk, A. Orthen, A. Sarvestani, A.H. Walenta, H. Walliser. On the dynamic two-dimensional charge diffusion of the interpolating readout structure employed in the MicroCAT detector, Nucl. Instr. and Meth. A 482 (2002) 334

- [19] M.J Berger, J.H. Hubbell, XCOM: Photon Cross Section Database, Ionizing Radiation Devision, National Institute of Standards and Technology, Gaithersburg, MD 20899 (1998)
- [20] S. Bachmann, A. Bressan, M. Capeáns, M. Deutel, S. Kappler, B. Ketzer, A. Polouektov, L. Ropelewski, F. Sauli, E. Schulte, L. Shekhtman, A. Sokolov. Discharge studies and prevention in the gas electron multiplier (GEM), Nucl. Instr. and Meth. A 479 (2002) 294
- [21] G.D. Alkhazov et al., Nucl. Instr. and Meth. 89 (1970) 155
- [22] U. Fano, Physical Review **72** (1947) 26
- [23] G.D. Alkhazov et al., Nucl. Instr. and Meth. 48 (1967) 1
- [24] G.D. Alkhazov et al., Nucl. Instr. and Meth. 75 (1969) 161
- [25] R.K. Sood, Z. Ye, R.K. Manchanda. Ultra-high pressure proportional counters Part II. Xenon, Nucl. Instr. and Meth. A 344 (1994) 384
- [26] T.G. Feige. Untersuchung systematischer Effekte auf die Energieauflösung in abbildenden Hochdruckzählern, Diploma Thesis, Siegen (1995)
- [27] V. Radeka. Low-noise techniques in detectors, Ann. Rev. Nucl. Part. Sci. 38 (1988) 217
- [28] C.M. Ma et al. MIT Technical Report 129 (1982), in: J. Fehlmann, G. Viertel. Compilation of Data for Drift Chamber Operation, ETH-Report (1983)
- [29] S.F. Biagi. Monte Carlo simulation of electron drift and diffusion in counting gases under the influence of electric and magnetic fields, Nucl. Instr. and Meth. A 421 (1999) 234
- [30] Magboltz, CERN Transport of Electrons in Gas Mixtures Computation Program written by S.F. Biagi, Version 2 (2002)
- [31] Maxwell 3D Field Simulator Version 5.0.04, Ansoft Corporation, Pittsburgh, PA USA (2002)